JOURNAL OF GEOPHYSICAL RESEARCH, VOL. 112, A09305, doi:10.1029/2007JA012524, 2007

Spatio-temporal characterization of the equatorial electrojet from CHAMP, Ørsted, and SAC-C satellite magnetic measurements

Patrick Alken[1,2,3] and Stefan Maus[2,3]

Received 4 May 2007; revised 20 June 2007; accepted 12 June 2007; published 13 September 2007.

[1] The equatorial electrojet (EEJ) is an eastward electric current on the day-side, flowing in a narrow band along the dip equator in the ionospheric *E* region. Recent magnetic observations from the CHAMP, Ørsted, and SAC-C satellites, comprising more than 95,000 dip equator crossings from 1999 to 2006, have provided an unprecedented longitudinal coverage of the EEJ magnetic signature. We have used these data to construct an empirical model of the EEJ current climatological mean and day to day variability as a function of longitude, local time, season, and solar flux. Our model has been successfully verified against vertical drift data from the JULIA radar at Jicamarca. We have also used the EEJ observations to estimate the self-correlation of the EEJ, confirming short longitudinal correlation lengths of 15° and finding a temporal correlation length of 2.4 h. Our model's predictions of the eastward electric field and its standard deviation may provide useful input to various kinds of ionospheric simulations. Coefficients and software are available online at http://models.geomag.us/EEJ.html and http://www.earthref.org.

Citation: Alken, P., and S. Maus (2007), Spatio-temporal characterization of the equatorial electrojet from CHAMP, Ørsted, and SAC-C satellite magnetic measurements, *J. Geophys. Res.*, *112*, A09305, doi:10.1029/2007JA012524.

1. Introduction

[2] In the ionospheric *E* region, tidal winds drive currents during the daytime which, together with the magnetic field, cause the accumulation of positive and negative charges at the dawn and dusk terminators respectively, resulting in a strong eastward electric field along the magnetic equator. This gives rise to the Hall and Pederson currents, and *Cowling* [1933] showed that when a Hall current is restricted by the presence of boundaries, the effective (Cowling) conductivity parallel to the boundaries is significantly enhanced beyond the normal Pederson conductivity. It was later realized that the presence of low conducting layers above and below the *E* region are sufficient to drive this Cowling conductivity near the magnetic equator, giving rise to the equatorial electrojet (EEJ) [see *Heelis*, 2004; *Forbes*, 1981].

[3] The geomagnetic observatory at Huancayo facilitated the discovery of the EEJ and provided data for many early studies [*Bartels and Johnston*, 1940a, 1940b; *Chapman*, 1951; *Egedal*, 1947, 1948], which focused on explaining the mechanism behind the current flow. It was also discovered that the current sometimes reversed direction during certain morning and evening hours, which became known as the "counter-electrojet" [*Gouin and Mayaud*, 1967]. Physical models and theories were developed in the 1970s which studied the vertical (Hall) current flow, longitudinal and local time structure of the EEJ, and the effects of local winds on the EEJ [*Sugiura and Poros*, 1969; *Richmond*, 1973; *Forbes and Lindzen*, 1976]. There have since been many studies of the EEJ based on ground observatory data [*Arora et al.*, 1993; *Rigoti et al.*, 1999; *Doumouya et al.*, 1998, 2003], which further study its main characteristics (day-today and seasonal variability, longitudinal and local time structure, counter-electrojet, etc.). A new generation of satellite magnetic data provides a longitudinal and temporal coverage of the EEJ previously unattainable with ground based observations alone. In our study, we used data from the CHAMP, Ørsted, and SAC-C satellites from 1999 to 2006 comprising over 95,000 dip equator crossings, to characterize the EEJ in longitude and time, and we have created climatological models of the EEJ mean and variance.

[4] There have been previous attempts in creating EEJ models, both theoretical and empirical. Most theoretical approaches have assumed various current distributions and analyzed the resulting magnetic effects [*Forbush and Casaverde*, 1961; *Chapman*, 1951; *Fambitakoye and Mayaud*, 1976; *Onwumechili*, 1967; *Untiedt*, 1967]. The empirical study of *Doumouya et al.* [2003] is based on ground observatory data and cannot offer a complete characterization of the EEJ in longitude. The empirical model of *Onwumechili and Ezema* [1992] was based on

[1]Department of Physics, University of Colorado, Boulder, Colorado, USA.
[2]Cooperative Institute for Research in Environmental Sciences, University of Colorado, Boulder, Colorado, USA.
[3]National Geophysical Data Center, NOAA, Boulder, Colorado, USA.

0148-0227/07/2007JA012524$09.00

POGO satellite data and provided measurements of several important quantities (mean peak current density, mean total eastward current, mean latitudinal extent, etc.), but did not offer longitudinal or seasonal profiles of the EEJ. Furthermore, most previous studies have focused on fitting the observed magnetic data. Our approach instead was to invert the magnetic data to obtain the actual currents and fit a model to the current density. This allows us to model the eastward electric field in addition to the EEJ current, using an appropriate conductivity model. We believe this to be the first empirical model of the actual EEJ sheet current density.

[5] In section 2 we give an overview of the satellite models. In section 3 we discuss our validation of the models using vertical drifts. Finally, in section 4 we use the models to discuss the spatial and temporal self-correlation of the EEJ.

2. Climatological Model of the Equatorial Electrojet

[6] To construct a useful model of the equatorial electrojet, we investigate the mean value of the electrojet current, and its deviation from the mean. By deviation, we refer to the actual day to day variability of the current strength about its climatological mean. The mean and standard deviation are functions of the winds, electric field, and conductivity in the *E* region. Since the satellites do not directly measure these quantities, we must use other parameters. We found that the EEJ can be modeled with reasonable accuracy by using four parameters. They are longitude, local time, season, and solar flux. For a solar flux proxy, we use the same quantity defined in the Extreme UltraViolet flux model for Aeronomic Calculations (EUVAC) [*Richards*, 1994, p. 8986], which is defined as $P = (F10.7 + F10.7A)/2$, where F10.7 is a proxy for the daily solar flux at 10.7 cm wavelength, and F10.7A is the 81 day centered average of F10.7. The proxy P has been shown to better represent EUV intensities than F10.7 alone [*Liu et al.*, 2006]. The longitudinal and local time dependence of the current is readily apparent. But there are also significant peaks in the current during equinox and so the seasonal dependence is very important. Also, we find a clear linear relationship between the electrojet strength and solar flux. It has been shown that lunar tides have an effect on the EEJ strength [*Bartels and Johnston*, 1940a], however we have neglected these effects in the present study. We plan to incorporate lunar effects in our EEJ model in a future study.

2.1. Satellite Data

[7] Our three climatological models of the EEJ are based entirely on data obtained from the CHAMP, Ørsted, and SAC-C satellites. The CHAMP satellite was launched in July 2000 into a near polar circular orbit with an initial altitude of 454 km. It drifts slowly in local time, decreasing one hour every eleven days, and completes an orbit every 92 min. CHAMP has scalar and vector magnetometers which provided the data used for the current inversion.

[8] Ørsted was launched in February 1999 into a retrograde orbit with an apogee of about 850 km and a perigee of about 640 km. It also drifts slowly in local time, decreasing 0.88 min/day, and completes an orbit every 100 min. It carries the same scalar and vector magnetometers as CHAMP, but the orientation of the vector magnetometer is given by a less accurate star camera.

[9] SAC-C was launched in November 2000 into a polar circular orbit of altitude 702 km. Its orbit is sun-synchronous, so it stays at a fixed local time of about 10:25 AM. Consequently, it passes over the dip equator close to the peak EEJ strength. SAC-C only provides scalar magnetometer data.

[10] In a procedure similar to the one described by *Lühr et al.* [2004], we inverted the magnetic field readings to obtain the EEJ currents. This was first done by subtracting the POMME-3.1 model [*Maus et al.*, 2006] from the magnetic measurements, removing contributions from the core, mantle, crust, and magnetosphere. The remaining signal, on a geomagnetically quiet day, is a combination of Sq and the equatorial electrojet. A background Sq signal was fitted to the remaining signal outside a $\pm 12^\circ$ window around the dip equator and then subtracted to get a clean EEJ signal. Finally, we assumed line currents spaced at 0.5 degrees following constant corrected geomagnetic (CGM) latitude (defined as quasi-dipole coordinates by *Richmond* [1995]) up to the horizon on both sides of the satellite orbit at 108 km altitude above the geoid, and inverted the magnetic signal for the line current strength. This procedure does not yield the actual current density, but a height integrated sheet current density. Figure 1 shows sample magnetic signatures for several passes over the dip equator after subtracting the POMME-3.1 model and background Sq signal, and the resulting sheet current densities from the inversion process. We initially inverted all satellite passes over the dip equator, except for those which contained large data gaps. However, for the final EEJ model, we restricted our data to days with $Kp \leq 2$, and used only inversion results from the scalar satellite magnetometers. The vector magnetometer data from CHAMP and Ørsted were used to verify the scalar data, in particular to calibrate the zero level of the currents. Because of the more complete coverage of the scalar data, only these were used in the final model. As can be seen in Figure 1, the CHAMP data provides the cleanest EEJ signatures. Because its altitude is lower than the other two satellites, it can more sharply resolve the peak in the magnetic signature, and we believe the EEJ model resulting from CHAMP to be the most trustworthy of the three models we created. The SAC-C data contains much more noise than the other two satellites because of technical reasons.

2.2. The EEJ Mean

[11] We represent the mean sheet current density at the dip equator by

$$\mu(\phi, t, s, p) = \sum_{i=0}^{N_\phi} \sum_{j=0}^{N_t} \sum_{k=0}^{N_s} \sum_{l=0}^{N_p} a_{ijkl} u_i(\phi) v_j(t) w_k(s) y_l(p), \quad (1)$$

where ϕ is longitude, t is local time, s is season (day of year), and p is the solar flux proxy P defined previously. The coefficients a_{ijkl} were estimated by minimizing the misfit given by

$$\epsilon = \sum_i \left(J_i^{eq} - \mu(\phi_i, t_i, s_i, p_i)\right)^2, \quad (2)$$

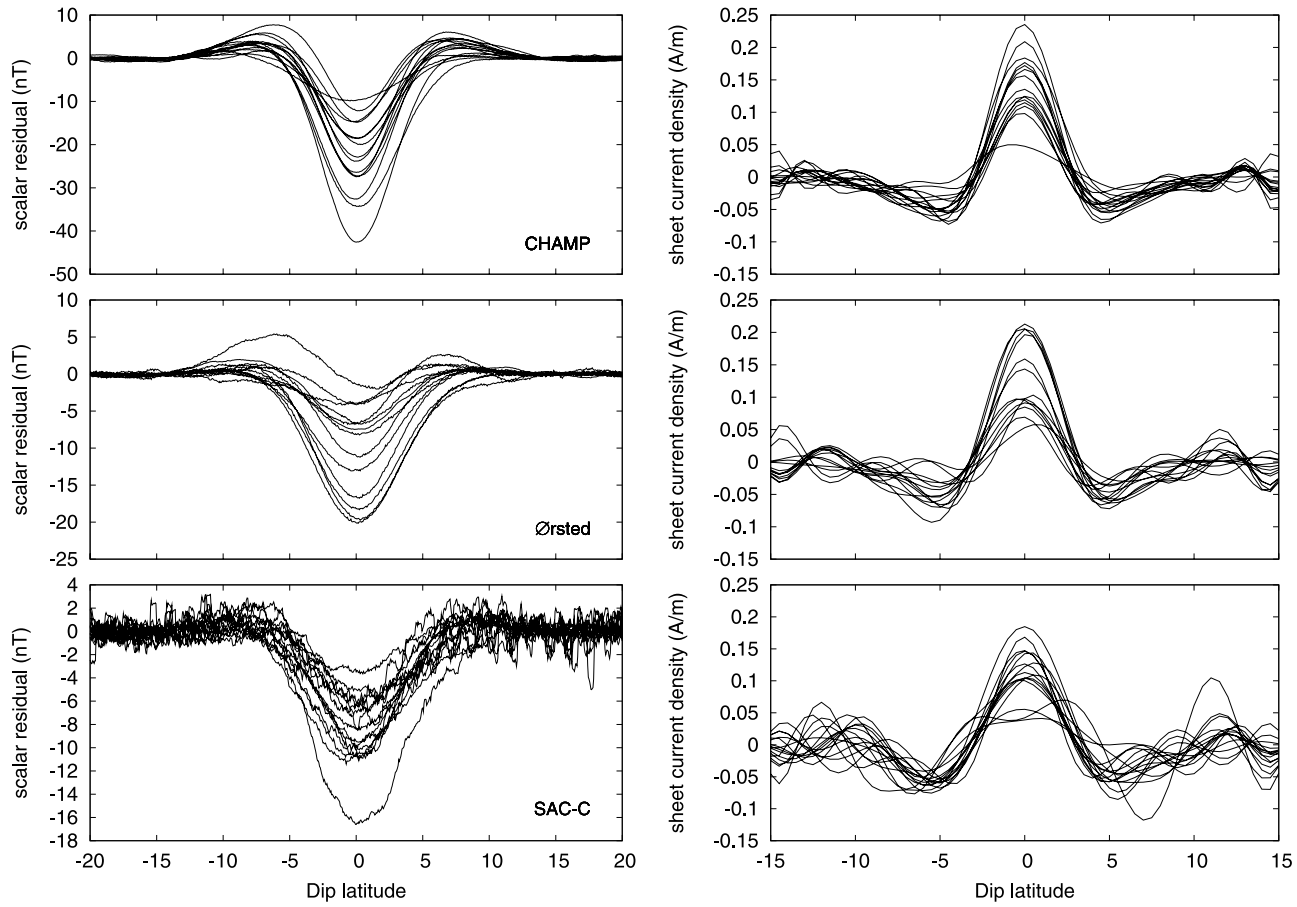

Figure 1. Left: magnetic field residuals after subtracting the POMME 3.1 model and the background Sq signal, showing all tracks for a single day in September 2001, when all three satellites were in the 10:00–11:00 local time sector. The CHAMP residuals are of higher quality and also stronger due to CHAMP's lower altitude. Right: EEJ signal after inverting magnetic data. For this study, we model the current value J^{eq} at the dip equator.

where J_i^{eq} is the current value at the dip equator. The basis functions are given by

$$u_i(\phi) = \begin{cases} \cos\left(\frac{i\phi}{2}\right) & \text{for i even} \\ \sin\left(\frac{(i+1)\phi}{2}\right) & \text{for i odd} \end{cases}$$
$$v_j(t) = B_j(t) \qquad (3)$$
$$w_k(s) = \begin{cases} \cos\left(\frac{2k\pi(s-s_0)}{365.25}\right) & \text{for k even} \\ \sin\left(\frac{2k\pi(s-s_0)}{365.25}\right) & \text{for k odd} \end{cases}$$
$$y_l(p) = p^l$$

The choice of basis functions is justified as follows: The longitudinal function $u_i(\phi)$ was chosen to be the standard sine and cosine representation which models well the periodicity in the longitude parameter. We chose $N_\phi = 8$ empirically to give a good fit in longitude. There was no natural basis function to use for the local time dependence, so we modeled this variable using cubic B-splines with uniform knots. We used the value $N_t = 7$. The seasonal basis function $w_k(s)$ was chosen based on the observation that the electrojet strength peaks at equinox and that there are differences between summer and winter. The value of the parameter s_0 is the day of the March equinox. The choice $N_s = 2$ provides a double peaked cosine for the peaks at March and September equinox, and a sine function for the summer/winter difference. Finally, because of the observed linear dependence of the electrojet on solar flux, we chose $N_p = 1$ which includes only a linear term in the fit.

2.2.1. Longitudinal Dependence of EEJ

[12] One of the interesting results of this model is the longitudinal profile of the EEJ, which was previously unattainable with ground based data alone. In Figure 2 (left) we plot 1-D longitudinal slices of the mean model for different seasons while holding local time and the solar flux proxy P fixed. During March and September equinox and June solstice we see a clear wave number-four signature of the EEJ. *England et al.* [2006] discuss this behavior, which they attribute to a wave number-four pattern in the diurnal tide, for a fixed local time. As discussed by *Forbes et al.* [2006], however, there is actually a wave number-three eastward propagating diurnal tide as viewed in a sun-fixed frame, but when it is viewed in a fixed local time frame

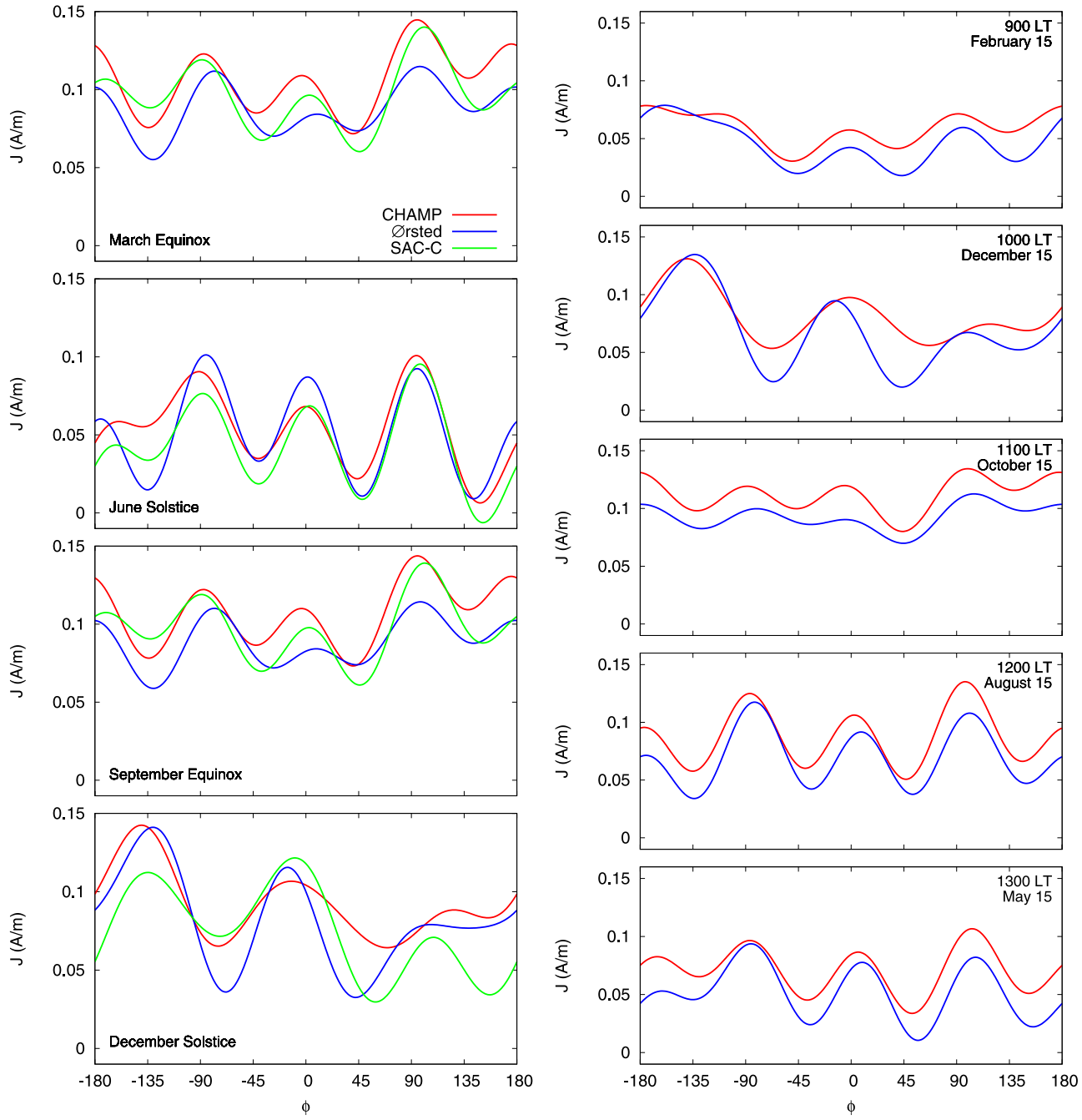

Figure 2. Left: Longitudinal dependence of EEJ for different seasons. These plots have local time fixed at 10:30 am, and P = 150 W/m^2. Right: Longitudinal dependence of EEJ for different local times and seasons. These plots have solar flux fixed at P = 150 W/m^2.

(a fixed location in the sun-fixed frame moving westward at one cycle per day), it appears as a wave number-four signature. During December solstice, we see a prominent wave number-three signature. It is reasonable to expect that this behavior is also due to the wind patterns, which we investigated using the wind model GSWM-02 [see *Hagan and Forbes*, 2002]. Since the EEJ is affected by winds in both the northern and southern hemispheres, we added the meridional wind speeds at 24° and −24° latitude to produce a signal which could be compared to the electrojet strength. The latitudes were chosen based on where the wind velocities peak, and the resulting signal contains information on the northern and southern winds which both contribute to the eastward electric field which drives the EEJ. The wind and EEJ profiles are taken at 12:00 LT along all longitudes. The results are shown in Figure 3. We do find a wave number-three structure in the winds during solstice. For reference, we also show the signals during March equinox. We see a significant phase shift between the two signals during solstice, and a smaller shift during equinox. To

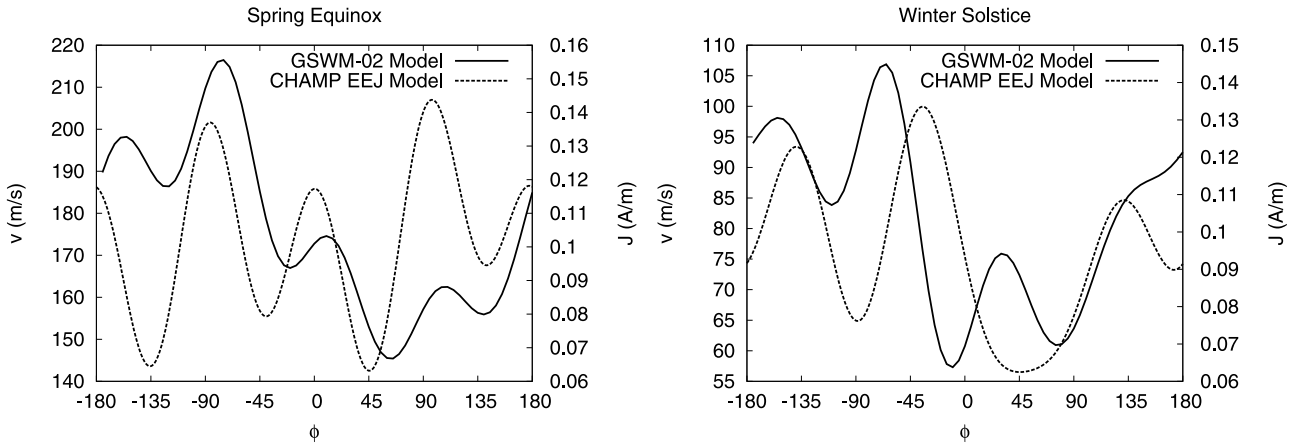

Figure 3. Left: Longitudinal dependence of EEJ and diurnal winds for March (equinox) conditions. We see the wave number-four structure in both signals. Right: Longitudinal dependence of EEJ and diurnal winds for December (solstice) conditions. The wave number-three structure in the EEJ is also present in the winds, but with significant phase shift.

explain these shifts, one would have to take the global wind field into account, rather than just the wind at the longitude of the EEJ measurement.

[13] In Figure 2 (right) we plot the longitudinal dependence for different local times and seasons with fixed solar flux. The local times and seasons were chosen to compare our results with the study of *Jadhav* [2002, Figure 6], which was based on Ørsted satellite data. The SAC-C model is not shown since it is valid only for local times near 10:30. We find the same general features in the longitudinal dependence of the EEJ. The peak around 0°E is present at all seasons and local times considered, while the peak at 90°W disappears during winter months. The previous study also finds a wave number-three structure during December. Finally, they find a large peak around 180°E from 8:30–9:30LT during January–March and another large peak around 270°E from 12:30–13:30 LT during April–June. While these peaks are present in our model also, we do not find such large magnitudes.

2.2.2. Local Time Dependence of EEJ

[14] In Figure 4 we plot the local time dependence of the EEJ for different longitudes and seasons. For different longitudes, the current follows the same basic pattern. Near sunrise, we see significant westward, counter-electrojet currents. Then the current rises sharply to a maximum between 10:30–12:00 LT, and gradually decreases and dies out at around 18:00 LT.

[15] We find that during solstice, the EEJ peak is significantly weaker than during equinox, and also peaks closer to local noon. These results are in good agreement with the empirical model of *Doumouya et al.* [2003]. The SAC-C model is not shown here since the satellite does not drift in local time.

2.2.3. Seasonal Dependence of EEJ

[16] As discussed previously, the EEJ is significantly stronger during equinox than during solstice. *Tarpley* [1973] explains this behavior in terms of seasonal shifts of the Sq foci. He demonstrates that the foci of the Sq current system in both the northern and southern hemispheres shift toward the equator during equinox, and shift toward the poles during solstice. This explains the strengthening and weakening of the EEJ during these seasons. Since the total eastward current between the foci is roughly the same throughout all seasons, as the foci shift equatorward during equinox, the EEJ intensity will increase. As the foci shift poleward during solstice, the EEJ intensity decreases. We plot the seasonal dependence of the EEJ for all three satellites in Figure 5 for several different longitudes. The maxima at equinox and minima at solstice are present for all longitudes. In several cases we see that the SAC-C and CHAMP models match up well but Ørsted does not. We attribute this to the fact that Ørsted drifts very slowly in local time, and so there is very little separation between seasonal and local time effects. Because season and local time are not really independent parameters in the Ørsted model, their independent effects could be mapped into each other, causing disagreements with the other two models.

2.3. The EEJ Deviation

[17] As discussed in section 2.2, we also created a climatological model of the EEJ temporal variability as given by its standard deviation from the climatological mean. To do this, we took each EEJ current data point and subtracted the climatological mean model we discussed above. This produced the dataset used to fit the deviation model, which represents the actual day to day variability of the EEJ. We used the same fitting procedure and basis functions as for the mean fit. Plots of the EEJ mean and its deviation from the CHAMP satellite are shown in Figure 6. As can be seen, the day to day variability of the EEJ is significant.

3. Verifying the Model Against Vertical Drifts

[18] To validate our equatorial electrojet model, we predicted mean vertical drifts at the JULIA radar location at Jicamarca near Lima, Peru, and then compared the predictions with the actual drift data taken. JULIA is a coherent scatter radar data acquisition system which uses the main

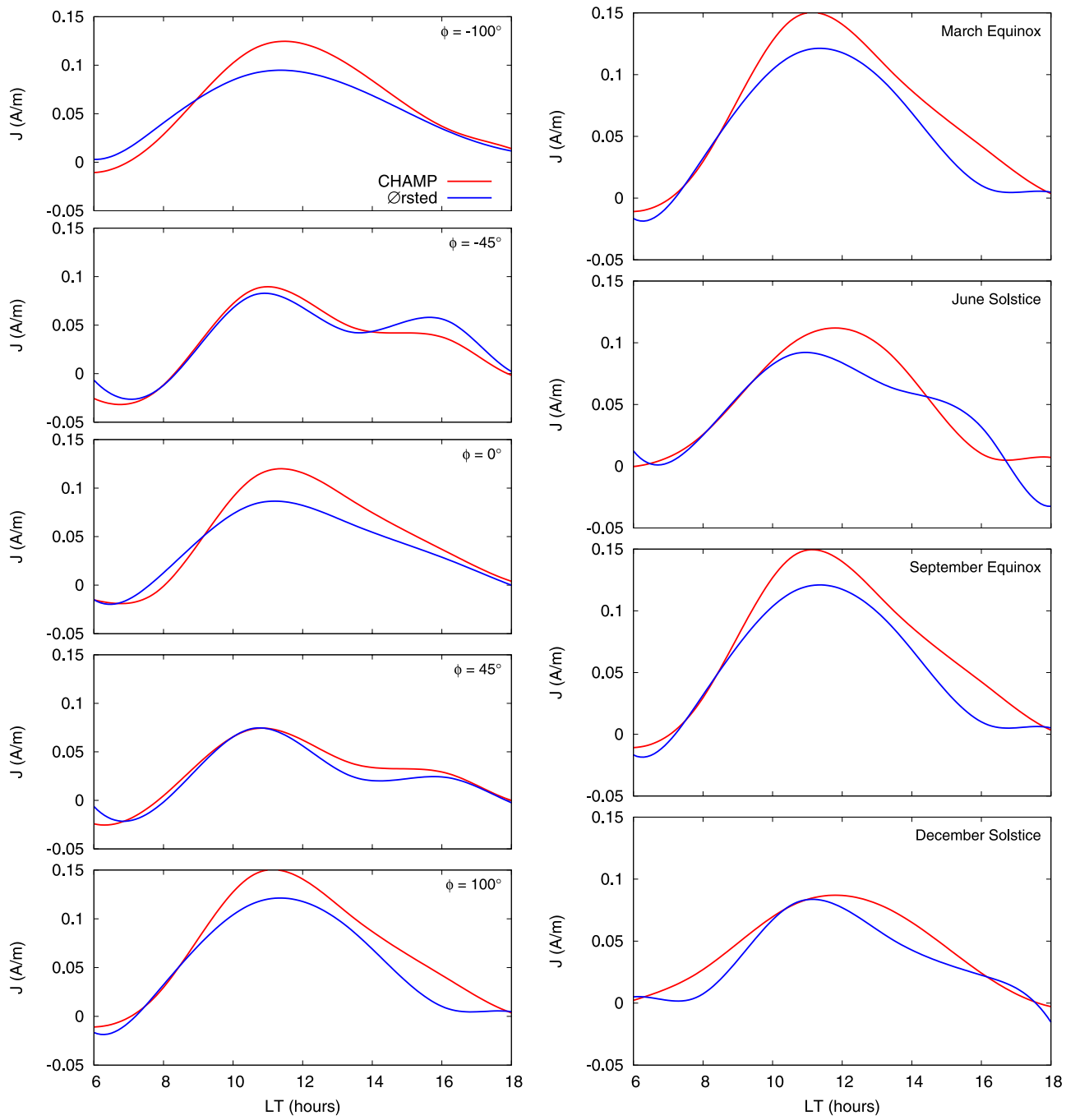

Figure 4. Left: Local time dependence of EEJ for different longitudes. These plots are all taken at March equinox, with $P = 150$ W/m^2. The longitude values were chosen to well represent the positions of the peaks and troughs in Figure 2 during March equinox. Right: Local time dependence of EEJ for different seasons. These plots have longitude fixed at 100°, and $P = 150$ W/m^2.

Jicamarca antenna array to make high quality measurements of 150 km drift echoes. Positive values of these echoes correspond to negative Doppler shifts, and thus upward drift motion [*Hysell et al.*, 1997]. The vertical drift data is typically available from about 10:30 LT to about 16:00 LT. To relate the EEJ to the vertical drifts, we estimate an effective height-integrated conductivity, which we describe below.

3.1. Conductivity Model

[19] *Robinson and Vondrak* [1984] derive the conductivity relations

$$\sigma_p = a_p[S_a \cos(\chi)]^b \tag{4}$$

$$\sigma_h = a_h[S_a \cos(\chi)]^b \tag{5}$$

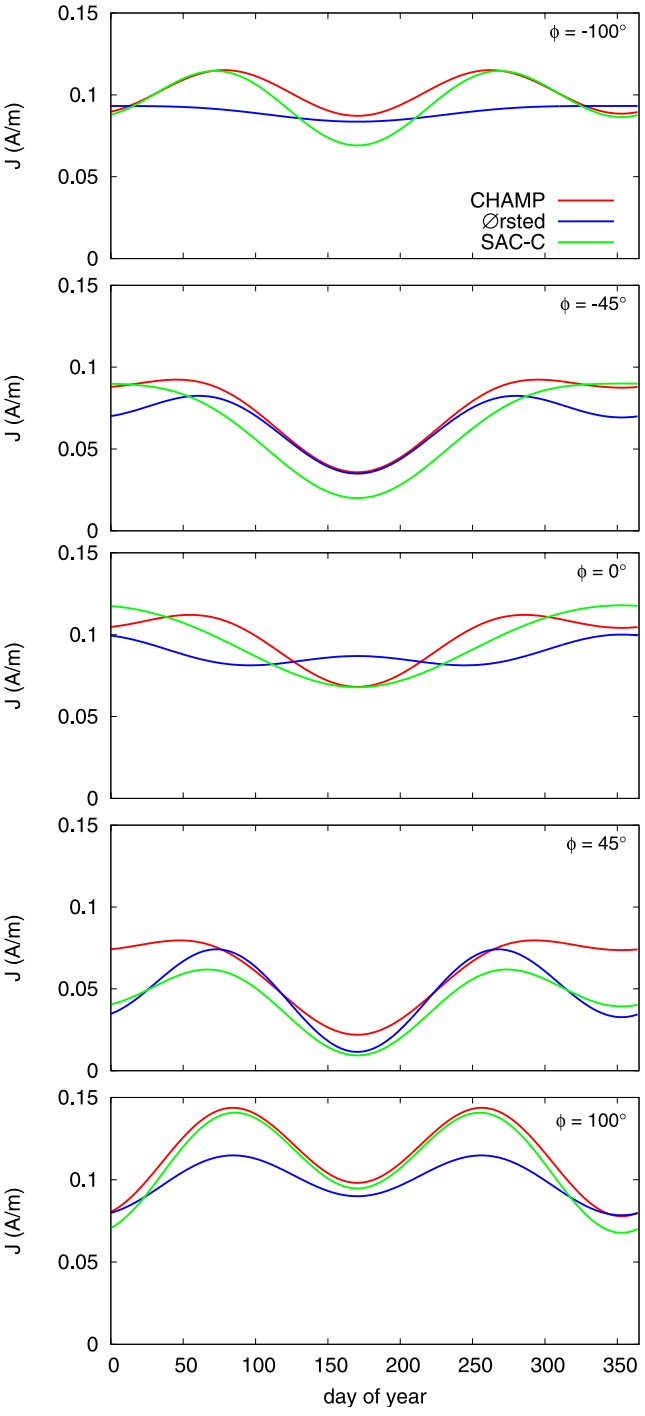

Figure 5. Seasonal dependence of EEJ for different longitudes. These plots have local time fixed at 10:30 am, and P = 150 W/m^2. The longitude values were chosen to well represent the position of the peaks and troughs of the longitudinal profiles from Figure 2.

for the Pederson and Hall conductivities, where χ is the solar zenith angle, S_a is the F10.7 value, and the parameters a_h, a_p, and b are to be determined by fitting data. In analogy, we model the effective conductivity σ_e as:

$$\sigma_e(\chi, S_a) = a_e[S_a \cos(\chi)]^b, \quad (6)$$

where we are using the solar flux proxy P for S_a instead of F10.7. This is a model with two parameters (a_e, b) that have to be estimated.

[20] To determine these parameters, we picked all CHAMP current measurements taken within ±5 degrees longitude of the JULIA radar. We then took all JULIA

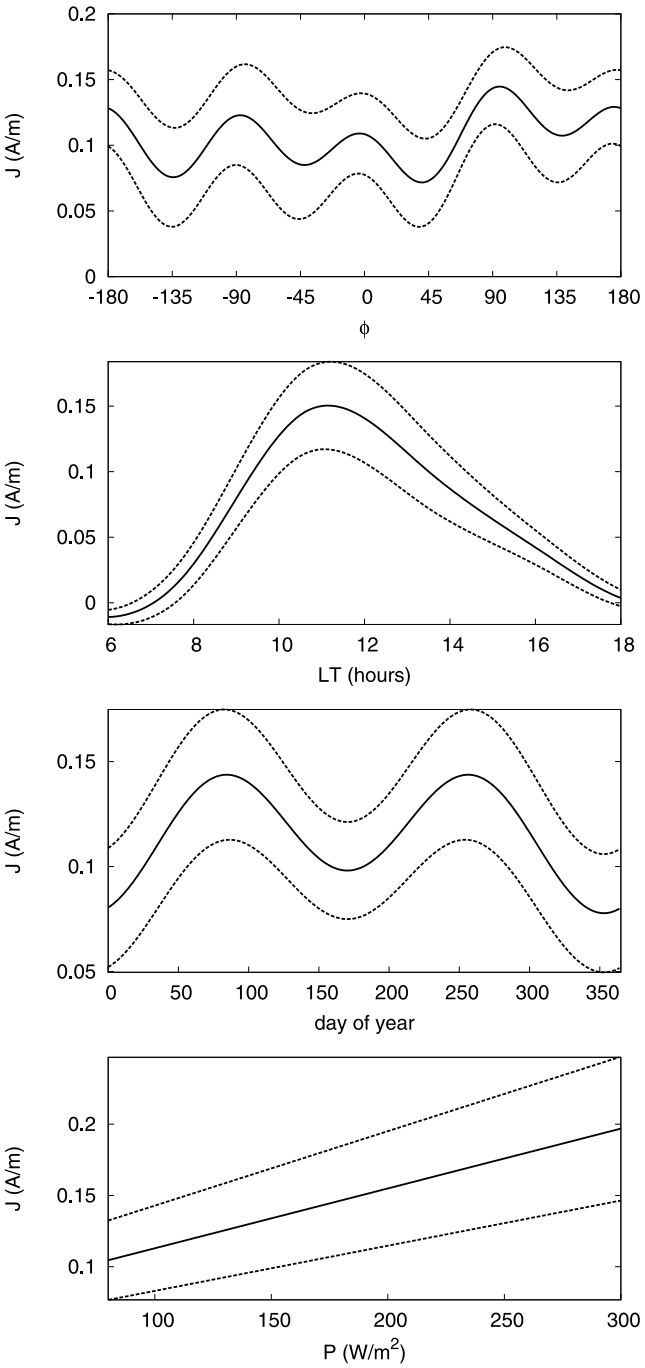

Figure 6. EEJ means (solid) with standard deviation curves (dashed) plotted against all four model parameters for the CHAMP satellite. The standard deviations indicate the typical daily variability of the EEJ strength. All plots except for the longitudinal dependence were generated for ϕ = 100°. Similarly, the other fixed parameters are local time: 10:30 am, season: March equinox, P: 150 W/m^2.

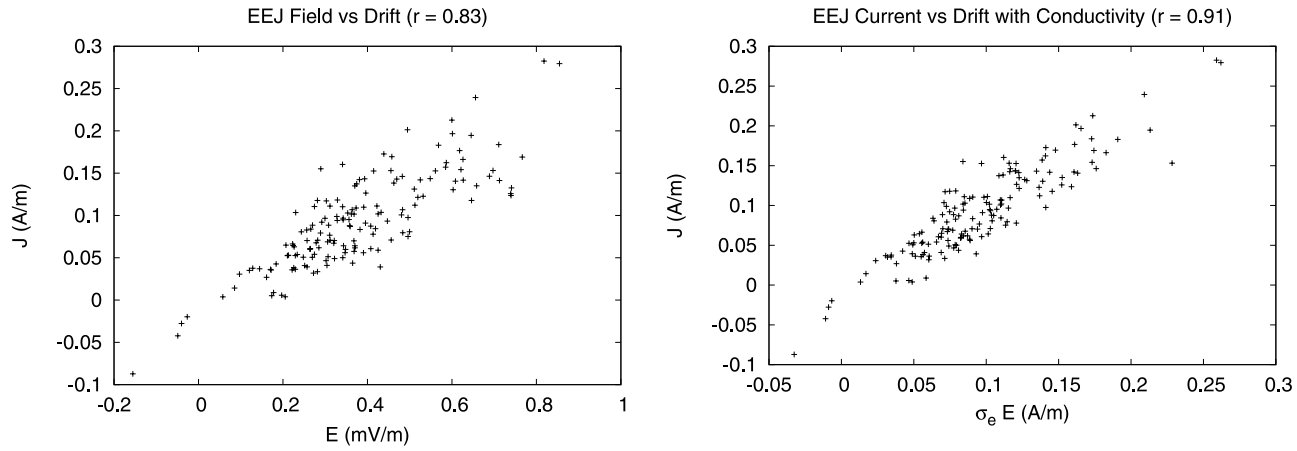

Figure 7. Left: EEJ current against corresponding eastward electric field inferred from vertical drift without accounting for conductivity. Right: EEJ current against drift-inferred electric field multiplied with effective conductivity. We find that the correlation improves from 0.83 to 0.91.

vertical drift measurements within ±20 min of the satellite pass and averaged them to get a drift velocity corresponding to our EEJ current measurement. We converted the drift value into an electric field value using the magnetic field intensity at 150 km above the JULIA radar. We then used the relation $J = \sigma_e E$ to least squares fit our data pairs to the σ_e model. This procedure yielded the values

$$a_e = 48.4 \tag{7}$$

$$b = 0.358 \tag{8}$$

where the units of a_e are such that σ_e has units of Siemens. The correlation of the original (J, E) data pairs was 0.83. As shown in Figure 7, our conductivity model improves this to 0.91.

3.2. Comparing the EEJ and Drift Models

[21] Using the σ_e model, we compared our climatological EEJ model from CHAMP with a climatological model of the vertical drifts at JULIA for all drift data taken from August 2001 to May 2006. The drift model was created using the same method as for the EEJ model, with a fixed longitude. The resulting model is a function of local time, season, and solar flux. We then sampled the two models over all parameter space (keeping longitude fixed in the EEJ model) and correlated the value of J with $\sigma_e E$. This procedure yielded a correlation coefficient of 0.93. We also computed the RMS error between the models defined as

$$\epsilon_{rms} = \sqrt{\frac{1}{V}\int\left(\frac{J(\mathbf{m})}{\sigma_e(\mathbf{m})B} - v(\mathbf{m})\right)^2 d\mathbf{m}} \tag{9}$$

where $\mathbf{m}$ represents the model parameters and is integrated over all of parameter space of volume V. $v(\mathbf{m})$ is the vertical drift velocity model derived from JULIA data, $J(\mathbf{m})$ is the mean EEJ model derived from CHAMP data, and $\sigma_e(\mathbf{m})$ is the effective conductivity model described in section 3.1. B is taken to be the magnetic field intensity at 150 km above the JULIA radar. We found ϵ_{rms} = 2.3 m/s, which corresponds to 55.8 $\mu V/m$ uncertainty in the climatological mean of the eastward electric field predicted by our EEJ model.

4. Electrojet Self-Correlation

[22] Using the models of the mean and standard deviation of the EEJ, we can address the interesting question of finding the correlation lengths of the EEJ in both longitude and time. The correlation of the EEJ with itself in longitude has been studied by *Manoj et al.* [2006] by correlating data from ground based observatories and the CHAMP satellite. However, the satellite based models of the EEJ mean and standard deviation make it possible to correlate the EEJ with itself in time as well. First, in analogy with the one-dimensional Pearson correlation coefficient [*Weatherburn*, 1962, p. 72], we define a two-dimensional correlation function as

$$r(d\phi, dUT) = \frac{1}{N}\sum_{i=1}^{N}\frac{J_i^{(1)} - \mu^{(1)}\left(\phi_i^{(1)}, t_i^{(1)}, s_i^{(1)}, p_i^{(1)}\right)}{\sigma^{(1)}\left(\phi_i^{(1)}, t_i^{(1)}, s_i^{(1)}, p_i^{(1)}\right)} \times \frac{J_i^{(2)} - \mu^{(2)}\left(\phi_i^{(2)}, t_i^{(2)}, s_i^{(2)}, p_i^{(2)}\right)}{\sigma^{(2)}\left(\phi_i^{(2)}, t_i^{(2)}, s_i^{(2)}, p_i^{(2)}\right)} \tag{10}$$

where the J_i are the sheet current densities from the inversion procedure discussed in section 2, μ is the climatological mean EEJ model, and σ is the climatological deviation model. The superscripts 1 and 2 refer to two different satellites; in our analysis we correlated the CHAMP and Ørsted satellite data. This equation is analogous to the standard Pearson correlation, however since each satellite data point J_i was measured at a specific longitude, local time, season, and solar flux, we subtract the EEJ mean and divide by its deviation using our climatological models for those specific parameters. The N pairs ($J_i^{(1)}$, $J_i^{(2)}$) occur when the two satellites both cross the electrojet at a fixed longitudinal separation $d\phi$ and at a fixed time separation dUT. This represents the correlation coefficient between the electrojet strength at one point,

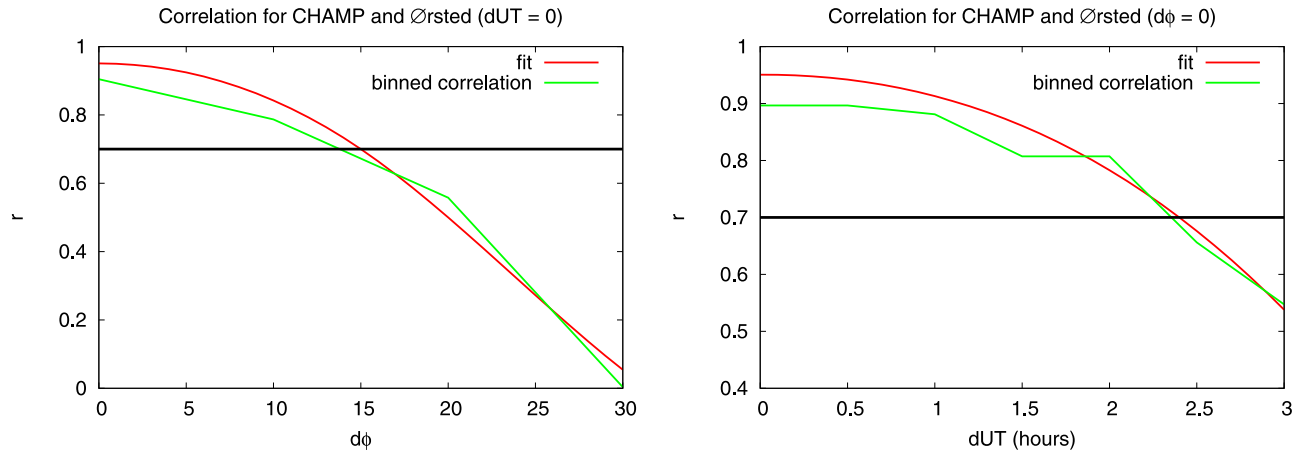

Figure 8. Left: In red, the correlation fit of CHAMP and Ørsted as a function of longitudinal separation for dUT = 0. In green, a correlation of the raw data with $|dUT|$ less than 60 min and longitudinal bin size of 10°. Right: In red, the correlation fit of CHAMP and Ørsted as a function of temporal separation for $d\phi = 0$. In green, a correlation of the raw data with $|d\phi|$ less than 10° and a temporal bin size of 60 min.

and its strength at a different point $d\phi$ away in longitude and dUT away in time. The values $J_i^{(1)}$ were measured by CHAMP and the values $J_i^{(2)}$ were measured by Ørsted which crossed the electrojet at some $d\phi$ and dUT away from the CHAMP crossing. Since the mean and deviation models were constructed from all available satellite data (with Kp ≤ 2), the correlation is not guaranteed to peak at 1, since for a given $d\phi$ and dUT, the N data pairs $(J_i^{(1)}, J_i^{(2)})$ are a small subset of the total satellite data set.

[23] An alternative way to define the EEJ self-correlation, would be to simply bin the data pairs $(J_i^{(1)}, J_i^{(2)})$ using a four-dimensional grid in longitude, local time, season, and solar flux, and then compute the standard correlation coefficient of each bin. However, we found that there are simply not enough data pairs to populate the bins for reasonable bin sizes, and therefore it is not possible to obtain a meaningful correlation with this method. Our approach above avoids this problem by using the previously calculated models as estimates of the mean and deviation for each satellite data measurement.

[24] Since there are not enough satellite data to compute equation (10) directly for every possible $(d\phi, dUT)$, we used a fitting procedure to approximate the true correlation. We can assume that the correlation function can be expanded in a basis as follows:

$$r(d\phi, dUT) = \sum_{i=0}^{N_{d\phi}} \sum_{j=0}^{N_{dUT}} r_{ij}\alpha_i(d\phi)\beta_j(dUT), \qquad (11)$$

where the coefficients r_{ij} are to be determined by least squares fitting. We used cubic B-splines for both basis functions $\alpha_i(d\phi)$ and $\beta_j(dUT)$, with $N_{d\phi} = 9$ and $N_{dUT} = 7$. We allow all possible longitudinal separations of the satellites, but restrict the temporal separation dUT to be within 6 h, which we found was large enough for the correlation to drop well below statistical significance.

[25] To construct this fit, we first selected all data from both satellites with Kp ≤ 2, and with a local time between 9am and 3pm. The local time interval was chosen so that there is a significant electrojet signal to correlate, to avoid correlating counter-electrojet events, and to avoid numerical problems with correlating noise. Once this data was selected, we picked out crossing events. A crossing event occurs when the two satellites cross the electrojet within 6 h of each other. When this occurs, the pair $(J^{(1)}, J^{(2)})$ was added to the dataset used to estimate the correlation. Using the CHAMP and Ørsted satellites for the correlation, this procedure yielded about 18,000 crossing pairs. We then used a least squares procedure to compute the r_{ij} coefficients of the fit. To verify the results, we also computed a correlation curve by binning the $(d\phi, dUT)$ data used for the fit and correlating the current pairs in each bin. The $d\phi$ bin size was 10° and the dUT bin size was 60 min. We used this as our control curve to compare to the fit. They are in good agreement, and the resulting curves are shown in Figure 8.

[26] In longitude, the correlation drops to 0.7 after 15° separation, which is in good agreement with the study of *Manoj et al.* [2006] who correlated ground data and CHAMP satellite data and also found a correlation of 0.7 after about 15° longitudinal separation. In time, our correlation drops to 0.7 after about 2.4 h.

5. Conclusion

[27] We have constructed climatological models of the Equatorial Electrojet based on satellite data from CHAMP, Ørsted, and SAC-C. The models are based on data which comprise half of a solar cycle (from solar maximum to solar minimum). The models exhibit the well known wave number-four longitudinal structure at equinox, and we find a wave number-three structure at December solstice, which we show is also present in the meridional diurnal winds. The models predict mean vertical drifts at the JULIA radar to within about 2.3 m/s, corresponding to 55.8 $\mu V/m$ uncertainty in the eastward electric field. We therefore believe the models will be useful in predicting mean electric fields along the magnetic equator as a function of longitude, local time, season, and solar flux. We also used the models

to compute the self-correlation of the EEJ and found short spatial and temporal correlation lengths of about 15° and 2.4 h, respectively.

[28] The model is available online (coefficients and driver program) at http://models.geomag.us/EEJ.html and http://www.earthref.org.

[29] **Acknowledgments.** We thank Claudia Stolle and Hermann Lühr for their helpful comments on an earlier version of this manuscript. The operational support of the CHAMP mission by the German Aerospace Center (DLR) and GeoForschungsZentrum are gratefully acknowledged. The Ørsted and SAC-C projects received extensive support from the Danish government, the Argentine Commission on Space Initiatives, NASA, ESA, CNES and DARA.

[30] Wolfgang Baumjohann thanks Arthur Richmond and another reviewer for their assistance in evaluating this paper.

References

Arora, B. R., M. V. Mahashabde, and R. Kalra (1993), Indian IEEY geomagnetic observational program and some preliminary results, *Braz. J. Geophys.*, *11*, 365–384.

Bartels, J., and H. F. Johnston (1940a), Geomagnetic tides in horizontal intensity at Huancayo, p. I, *J. Geophys. Res.*, *45*, 269–308.

Bartels, J., and H. F. Johnston (1940b), Geomagnetic tides in horizontal intensity at Huancayo, p. II, *J. Geophys. Res.*, *45*, 485–512.

Chapman, S. (1951), The equatorial electrojet as detected from the abnormal electric current distribution above Huancayo, Peru, and elsewhere, *Arch. Meteorol. Geophys. Bioclimatol., Series A*, *4*, 368–390.

Cowling, T. G. (1933), The electrical conductivity of an ionized gas in the presence of a magnetic field, *Mon. Not. R. Astron. Soc.*, *93*, 90–98.

Doumouya, V., J. Vassal, Y. Cohen, O. Fambitakoye, and M. Menvielle (1998), The equatorial electrojet: First results from magnetic measurement, *Annales de Geophysicae*, *16*, 658–676.

Doumouya, V., Y. Cohen, B. R. Arora, and K. Yumoto (2003), Local time and longitude dependence of the equatorial electrojet magnetic effects, *J. Atmos. Sol. Terr. Phys.*, *65*, 1265–1282.

Egedal, J. (1947), The magnetic diurnal variation of the horizontal force near the magnetic equator, *Terr. Magn. Atmos. Electr.*, *52*, 449–451.

Egedal, J. (1948), Daily variation of the horizontal magnetic force at the magnetic equator, *Nature*, *161*, 443–444.

England, S. L., S. Maus, T. J. Immel, and S. B. Mende (2006), Longitudinal variation of the E-region electric fields caused by atmospheric tides, *Geophys. Res. Lett.*, *33*, L21105, doi:10.1029/2006GL027465.

Fambitakoye, O., and P. N. Mayaud (1976), The equatorial electrojet and regular daily variation S_R:-I. A determination of the equatorial electrojet parameters, *J. Atmos. Sol. Terr. Phys.*, *38*, 1–17.

Forbes, J. M. (1981), The equatorial electrojet, *Rev. Geophys. Space Physics*, *19*(3), 469–504.

Forbes, J. M., and R. S. Lindzen (1976), Atmospheric solar tides and their electrodynamic effects, *J. Atmos. Sol. Terr. Phys.*, *38*, 911–920.

Forbes, J. M., J. Russell, S. Miyahara, X. Zhang, S. Palo, M. Mlynczak, C. J. Mertens, and M. E. Hagan (2006), Troposphere-thermosphere tidal coupling as measured by the SABER instrument on TIMED during July–September 2002, *J. Geophys. Res.*, *111*, A10S06, doi:10.1029/2005JA011492.

Forbush, S. E., and M. Casaverde (1961), The equatorial electrojet in Peru, *Carnegie Institute Washington*, *Publ 620*.

Gouin, P., and P. N. Mayaud (1967), A propos de l'existence possible d'un "contre electrojet" aux latitudes magnetiques equatoriales, *Annales de Geophysicae*, *23*, 41–47.

Hagan, M. E., and J. M. Forbes (2002), Migrating and nonmigrating diurnal tides in the middle and upper atmosphere excited by tropospheric latent heat release, *J. Geophys. Res.*, *107*(D24), 4754, doi:10.1029/2001JD001236.

Heelis, R. A. (2004), Electrodynamics in the low and middle latitude ionosphere: A tutorial, *J. Atmos. Sol. Terr. Phys.*, *66*, 825–838.

Hysell, D. L., M. F. Larsen, and R. F. Woodman (1997), Julia radar studies of electric fields in the equatorial electrojet, *Geophys. Res. Lett.*, *24*(13), 1687–1690.

Jadhav, G., M. Rajaram, and R. Rajaram (2002), A detailed study of equatorial electrojet phenomenon using Ørsted satellite observations, *J. Geophys. Res.*, *107*(A8), 1175, doi:10.1029/2001JA000183.

Liu, L., W. Wan, B. Ning, O. M. Pirog, and V. I. Kurkin (2006), Solar activity variations of the ionospheric peak electron density, *J. Geophys. Res.*, *111*, A08304, doi:10.1029/2006JA011598.

Lühr, H., S. Maus, and M. Rother (2004), Noon-time equatorial electrojet: Its spatial features as determined by the CHAMP satellite, *J. Geophys. Res.*, *109*, A01306, doi:10.1029/2002JA009656.

Manoj, C., H. Lühr, S. Maus, and N. Nagarajan (2006), Evidence for short spatial correlation lengths of the noontime equatorial electrojet inferred from a comparison of satellite and ground magnetic data, *J. Geophys. Res.*, *111*, A11312, doi:10.1029/2006JA011855.

Maus, S., M. Rother, C. Stolle, W. Mai, S. Choi, H. Lühr, D. Cooke, and C. Roth (2006), Third generation of the Potsdam magnetic model of the earth (POMME), *Geochem. Geophys. Geosyst.*, *7*, Q07008, doi:10.1029/2006GC001269.

Onwumechili, C. A. (1967), *Geomagnetic variations in the equatorial zone of Peru Physics of Geomagnetic Phenomena-I*, 425–507 pp., Academic, Inc, New York, London.

Onwumechili, C. A., and P. O. Ezema (1992), Latitudinal and vertical parameters of the equatorial electrojet from an autonomous data set, *J. Atmos. Sol. Terr. Phys.*, *54*, 1535–1544.

Richards, P. G., J. A. Fennelly, and D. G. Torr (1994), EUVAC: A solar EUV flux model for aeronomic calculations, *J. Geophys. Res.*, *99*(A5).

Richmond, A. D. (1973), Equatorial electrojet - I. Development of a model including winds and electric field, *J. Atmos. Sol. Terr. Phys.*, *35*, 1083–1103.

Richmond, A. D. (1995), Ionospheric electrodynamics using magnetic apex coordinates, *J. Geomag. Geoelec.*, *47*, 191–212.

Rigoti, A., F. H. Chamalaun, N. B. Trivedi, and A. L. Padilha (1999), Characteristics of the equatorial electrojet determined from an array of magnetometers in N-NE Brazil, *Earth Planets Space*, *51*, 115–128.

Robinson, R. M., and R. R. Vondrak (1984), Measurements of E region ionization and conductivity produced by solar illumination at high latitudes, *J. Geophys. Res.*, *89*, 3951–3958.

Sugiura, M., and D. J. Poros (1969), An improved model equatorial electrojet with a meridional current system, *J. Geophys. Res.*, *74*, 4025–4034.

Tarpley, J. D. (1973), Seasonal movement of the Sq current foci and related effects in the equatorial electrojet, *J. Atmos. Sol. Terr. Phys.*, *35*, 1063–1071.

Untiedt, J. (1967), A model of the equatorial electrojet involving meridional currents, *J. Geophys. Res.*, *72*(23).

Weatherburn, C. E. (1962), *A first course in mathematical statistics*, Cambridge Univ. Press, London.

P. Alken, National Geophysical Data Center, NOAA E/GC1, 325 Broadway, Boulder, CO 80305-3328, USA. (patrick.alken@noaa.gov)

S. Maus, Cooperative Institute for Research in Environmental Sciences, University of Colorado, Boulder, CO, USA.